Electric field measurements in the inner magnetosphere by Cluster EDI

H. Matsui, J. M. Quinn, R. B. Torbert, and V. K. Jordanova
Space Science Center, University of New Hampshire, Durham, New Hampshire, USA

W. Baumjohann
Institut für Weltraumforschung der Österreichischen Akademie der Wissenschaften, Graz, Austria

P. A. Puhl-Quinn and G. Paschmann
Max-Planck-Institut für extraterrestrische Physik, Garching, Germany

Received 26 February 2003; revised 21 June 2003; accepted 1 July 2003; published 30 September 2003.

[1] We report electric field measurements in the inner magnetosphere from the Electron Drift Instrument (EDI) on Cluster at distances of $4 < L < 10$. The data used in this study span more than 1 year so that all local times are covered. Both components of the electric field perpendicular to the ambient magnetic field are mapped into the equatorial plane with the magnetic field model of *Tsyganenko and Stern* [1996]. Average values and standard deviations are sorted by the polarity of the B_Z component of the interplanetary magnetic field (IMF). Average *Kp* values for both B_Z polarities are 1.45 ($B_Z > 0$) and 2.45 ($B_Z < 0$). These electric fields are discussed in terms of their sources such as the ionospheric dynamo and the solar wind-magnetosphere interaction. We also quantify the electric field as follows: the average shielding parameter γ [*Volland*, 1973; *Stern*, 1975] is $\sim$2, although the value for southward IMF is smaller than the value for northward IMF. The parameter γ is larger on the duskside than in the dawn sector. The average rate of sunward transport of magnetic flux, equivalent to the duskward electric field, is estimated as 0.32 mV/m for southward IMF. Finally, fluctuations tend to be larger than the DC component around the stagnation point, which could lead to outflow of plasmaspheric material. *INDEX TERMS:* 2712 Magnetospheric Physics: Electric fields (2411); 2730 Magnetospheric Physics: Magnetosphere—inner; 2736 Magnetospheric Physics: Magnetosphere/ionosphere interactions; 2784 Magnetospheric Physics: Solar wind/magnetosphere interactions; *KEYWORDS:* electric fields, inner magnetosphere, electron drift instrument

Citation: Matsui, H., J. M. Quinn, R. B. Torbert, V. K. Jordanova, W. Baumjohann, P. A. Puhl-Quinn, and G. Paschmann, Electric field measurements in the inner magnetosphere by Cluster EDI, *J. Geophys. Res.*, *108*(A9), 1352, doi:10.1029/2003JA009913, 2003.

1. Introduction

[2] The magnetospheric electric field is a subject of scientific research for more than 40 years because it plays an important role for the transport of plasma by the $E \times B$ drift motion. In the pioneer works of *Dungey* [1961] and *Axford and Hines* [1961], the convection electric field driven by the solar-wind magnetosphere interaction is inferred in order to explain the equivalent current system from ground magnetometers. Interaction via reconnection is discussed in the former, while viscous interaction is discussed in the latter. *Nishida* [1966] takes into account the corotating effect in addition to the above electric field in order to explain the formation of the plasmasphere. The location of the plasmapause is determined by the balance between the convection field and the corotation field. The latter is constant, while the former varies depending on the solar wind condition. In addition, it is necessary to consider magnetosphere-ionosphere coupling. The conductivity along the magnetic field line is very large so that the electric potential difference between the two regions over large scale sizes is assumed to be zero. Hence the magnetospheric ring current, field-aligned current, and ionospheric conductivity are important factors to determine the magnetospheric electric field as suggested by, e.g., *Vasyliunas* [1970, 1972] and *Jaggi and Wolf* [1973]. At the inner boundary of the ion plasmasheet, the gradient of the electric field tangential to the boundary is related to the field-aligned current. This current is closed with the ionospheric current. When we consider the balance between these currents, the electric field inside the inner edge is weaker than the electric field at regions outside of it. As a result, the convection electric field tends to be shielded inside this edge, namely the Alfvén layer. This effect depends on the geomagnetic activity.

[3] In a later study, *Galperin et al.* [1974] found an enhancement of the electric field at subauroral latitudes during magnetic storms. This electric field is now called

0148-0227/03/2003JA009913$09.00

subauroral polarization streams (SAPS) [*Foster and Burke*, 2002] and is caused by the charge separation at the inner edge of the electron plasma sheet, since plasma sheet ions can penetrate further inside than electrons. The size of these electric fields is much larger than the convection field mentioned above. The potential created at the location of SAPS is comparable to the size of the polar cap potential [*Anderson et al.*, 2001].

[4] Part of the magnetospheric electric field is driven by the ionospheric dynamo [*Baumjohann et al.*, 1985]. Although its amplitude is small, it is prominent in regions closer to the Earth during quiet geomagnetic activity. Typically, the AC component of electric fields are reported as Pc 5 pulsations [e.g., *Junginger et al.*, 1984] and irregular oscillations [e.g., *Quinn et al.*, 1999]. These oscillating components are known to be comparable in size to the DC component, so they may have an important effect on the transport of the plasmas.

[5] That magnetospheric convection electric fields play a predominant role in ring current energization and trapping was demonstrated by *Jordanova et al.* [1998]. In this study, ring current development was simulated using a global kinetic model with a time-dependent convection electric field and variable stormtime plasma inflow on the nightside. A good agreement between modeled and observed *Dst* values was achieved. *Jordanova et al.* [2001] studied effects of inner magnetospheric convection on ring current evolution during a storm by comparing results from two convection models. They found that the agreement between model simulations and data was better for one model than the other. These studies demonstrate the necessity of good knowledge of the electric field for reliable modeling of inner magnetospheric dynamics.

[6] Despite their obvious importance, the observations of the electric field are difficult. Before in situ measurements, the electric field was inferred from ground magnetometer records and the location of the plasmapause. From spacecraft, the electric field pattern was observed by the double probe on OGO 6 [*Heppner*, 1972]. *Maynard et al.* [1983] did a statistical analysis of the electric field inside the plasmasphere from ISEE 1 with an equatorial orbit. Recently, *Rowland and Wygant* [1998] reported statistics of the electric field from CRESS. They analyzed the dawn-dusk electric field component at $MLT = 1200 \sim 0400$ and $L = 2.5 \sim 8.5$. Case studies of the stormtime electric field from the same instrument are reported by *Wygant et al.* [1998] and *Burke et al.* [1998]. Electric fields have also been observed by double probes from polar orbiting spacecraft [e.g., *Heppner*, 1972; *Mozer et al.*, 1979; *Heppner and Maynard*, 1987; *Harvey et al.*, 1995; *Weimer*, 1995, 2001]. Measurement of the ion drift along the spacecraft trajectory is another technique to measure the electric field [*Heelis et al.*, 1976]. Ground-based measurements with incoherent scatter radars are also common [*Wand and Evans*, 1981; *Blanc and Amayenc*, 1979]. Movement of ducts of whistler paths enables estimates of the azimuthal electric field [*Carpenter and Seely*, 1976; *Carpenter et al.*, 1979]. For comparison of electric fields from all these techniques, the electric field should be mapped to the magnetosphere using magnetic field models.

[7] Apart from the above measurements, the electric field can also be measured by the so-called electron beam technique. In this case the electron drift motion is directly measured by the test beam so that it is possible to measure the two components of the electric field perpendicular to the magnetic field. This instrument was first flown aboard a geosynchronous satellite, Geos 2 [*Melzner et al.*, 1978], although its maximum time resolution was one spin period of 6 s. Both the DC component [*Baumjohann et al.*, 1985, 1986; *Baumjohann and Haerendel*, 1985] and the AC component [*Junginger et al.*, 1984] were analyzed. This instrument was also implemented on Geotail spacecraft [*Tsuruda et al.*, 1994, 1998; *Matsui et al.*, 2001]. Further development led to a time resolution much shorter than the spin period of the spacecraft [*Paschmann et al.*, 1997]. This improved Electron Drift Instrument (EDI) was first put aboard Equator-S [*Quinn et al.*, 1999; *Paschmann et al.*, 1999]. The same type of instrument was flown also on the Cluster spacecraft, which consist of four spacecraft (SC 1, 2, 3, and 4). Initial results from them are reported by *Paschmann et al.* [2001] and *Quinn et al.* [2001].

[8] In this study we analyze two components of the electric field data obtained by EDI on the Cluster spacecraft. As the Cluster spacecraft have polar orbits with perigees at $\sim 4\ R_E$ and apogees at $\sim 20\ R_E$, the spatial coverage is much more extensive than the previous observations by Geos 2. Based on these new types of data sets, we investigate the electric field at $4 < L < 10$, while convection in the tail lobe is investigated in a companion paper by *Noda et al.* [2003]. The data are organized by the polarity of the IMF B_Z. The inferred electric field pattern is discussed in terms of the shielding of the dawn-dusk electric field, transport of magnetic flux, and fluctuations compared to DC components.

[9] The organization of this paper is as follows. Data used in this study are described in detail in section 2. Two case studies of the electric field are shown in section 3. The first one is in the premidnight MLT sector, while the other one is in the afternoon MLT sector, so that different characteristics are illustrated between these two. Statistical results are shown for average features and standard deviations in section 4. These results are compared with previous electric field observations. Physical implications are discussed in section 5. Finally, conclusions are given in section 6.

2. Data

[10] In this study we use the electric field data from the Electron Drift Instrument (EDI) on Cluster. The hardware specification and principle of operation of the instrument are described in detail by *Paschmann et al.* [1997, 2001]. Here we discuss them briefly. The energy of the emitted beam from the electron gun is 500 eV or 1 keV. Electron motion consists of $E \times B$ drift and gradient B drift in addition to the gyration about the magnetic field line. We determine the electric field from the $E \times B$ drift motion. The contribution from the gradient B drift is not large in the available data as discussed later. There is no curvature drift because the electron beams are emitted in the direction perpendicular to the magnetic field. When the artificially emitted electrons come back to the detector, they are accompanied by the natural background electrons. The latter represents a quantity of available electrons with an energy of 500 eV or 1 keV with a pitch angle of 90°. In this study, data from SC 1, 2,

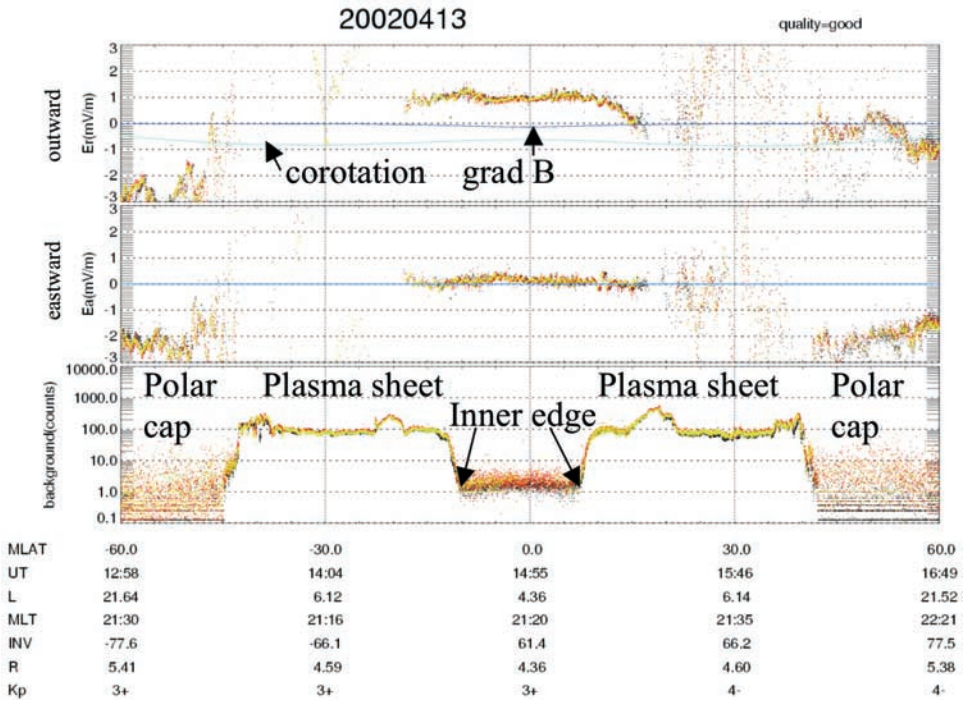

Figure 1. EDI data at premidnight MLT at $-60^\circ \sim 60^\circ$ MLAT on 13 April 2002. Data from three spacecraft are overlaid (SC 1: black, 2: red, 3: green). The top two panels show electric fields in the inertial and field-aligned coordinate system for two perpendicular components: outward and eastward. The light blue and dark blue lines show corotating and gradient B drifts estimated from Tsyganenko model. The bottom panel shows natural background electrons with an energy of 1 keV and with a pitch angle of 90°. Quantities other than MLAT in the bottom of the figure show those for SC 1.

and 3 are used. The EDI on SC 4 was not operating during the time interval analyzed. The time resolution of the original data set used in this study is 2 s. If there are no return beams on the detector, it is not possible to obtain the electric fields. Hence there are data gaps from time to time. When the raw data are processed, the quality of the data is tagged as good, caution, or bad. In this study only data with good quality are used. Moreover, we have removed data spikes which differ by more than 10 mV/m from their neighboring points because we can get a smoother result.

[11] We also use magnetic field and plasma data from ACE spacecraft as an upstream monitor of the solar wind [*Smith et al.*, 1998; *McComas et al.*, 1998]. The propagation delay is taken into account and 40 min averages are used. As for the mapping procedure, we use the magnetic field model of *Tsyganenko and Stern* [1996].

3. Case Studies

[12] We show data from two Cluster orbits to illustrate the electric field measured. One event includes data from the premidnight region, while the other includes data from the afternoon.

[13] Figure 1 shows the electric field data between -60° and 60° magnetic latitude (MLAT) on 13 April 2002. The quantities other than MLAT at the bottom of the figure are for SC 1. The difference in UT between times that SC 1, 2, and 3 pass through the same MLATs is within 1 min in this case. The average value of the interplanetary magnetic field (IMF) from ACE is $(B_Y, B_Z) = (-1.3, -3.6)$ nT so that the direction is southward, although the polarity of the 40 min average field changes from southward to northward at ~1615 UT. The geomagnetic activity is moderate. (*Kp* values are 3^+ and 4^-.) The top two panels show electric fields in the inertial and field-aligned coordinate system for two perpendicular components: outward and eastward. The data from three spacecraft are shown with the following colors: SC 1 (black), 2 (red), and 3 (green). The electric fields from the three spacecraft are similar to each other so that the electric field does not seem to have strong spatial gradients. Contributions from corotation and gradient B drift are calculated using the magnetic field model of *Tsyganenko and Stern* [1996]. Each contribution is shown with light blue and dark blue colors, respectively. The bottom panel in the figure shows background electrons, namely natural electrons, with an energy of 1 keV. From this panel, we can see that the spacecraft are earthward of the inner edge of the electron plasmasheet between -10° and 7° because of the lower count rate of the background electrons. At higher magnetic latitude, the spacecraft are in the plasmasheet. The count rates of electrons are high in this region. Beyond these latitudes, the spacecraft are in the polar cap because the electron count rates are close to zero.

[14] The electric field data within the inner edge indicate strong outward components. Their magnitude is approximately 1 mV/m in the inertial frame. If we take into account the corotating speed with −0.5 mV/m, the magnitude is as large as 1.5 mV/m in the corotating frame. This large electric field might result from the so-called subauroral polarization streams (SAPS) as defined by *Foster and Burke*

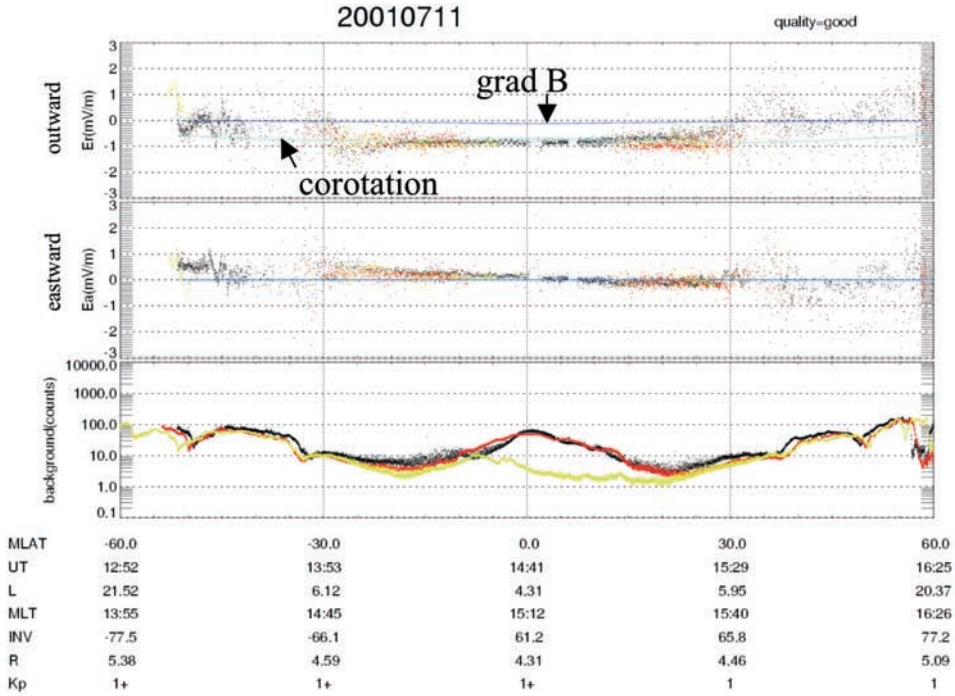

Figure 2. EDI data at postnoon MLT at $-60^\circ \sim 60^\circ$ MLAT on 11 July 2001. The format is the same as Figure 1.

[2002] or subauroral ion drifts (SAID). Here we should note that the effect of the gradient B drift is not large. The magnitude is at most ~0.1 mV/m around perigee, otherwise it is even smaller. As for the azimuthal component, the electric field around the inner edge is slightly eastward, which is consistent with the ground whistler observation by *Carpenter et al.* [1979]. The contribution from the corotating and gradient B drifts to the azimuthal component is negligible. At higher latitude in the plasmasheet with natural background electrons, the electric fields are continuous through ~15° MLAT. Beyond this latitude, the electric field is largely scattered, which indicates that strong wave components exist. When the spacecraft move further in the polar cap, the convection is not scattered. The direction is consistent with the two-cell convection pattern, although this point is beyond the scope of this study, which will concentrate on data at $L < 10$ ($-45.4 \sim 45.5$ MLAT in Figure 1).

[15] Figure 2 shows another event between -60° and 60° MLAT on 11 July 2001. The L value is less than 10 between -45.6 and 46.5 MLAT. The difference in UT between the times that SC 1, 2, and 3 pass through the same MLATs is within 40 min in this case. The IMF from ACE is $(B_Y, B_Z) = (-5.1, 1.4)$ nT. It is dawnward and northward. *Kp* values are 1^+ or 1 so that the geomagnetic condition is quiet. The top panel shows slightly inward component in reference to the corotating field around the perigee. The size is ~0.1 mV/m in the corotating frame. As the absolute value of the magnetic latitude increases to 30°, the sign of the radial electric field changes to outward. Although the electric field values are scattered, the approximate magnitude is 1 mV/m. As for the azimuthal component, the sign reverses around the magnetic equator: the direction is westward in the Northern Hemisphere and eastward in the Southern Hemisphere. When IMF B_Y has large negative values, the convection cell pattern is different between the two hemispheres. The dawnside cell becomes larger in the Northern Hemisphere, while the duskside cell becomes larger in the Southern Hemisphere. Such an effect might be canceled at the equator, which is consistent with the observation. It is more difficult to explain the reversal of the direction at the equator with the temporal variation of the convection during the equatorial passage of the spacecraft because the IMF is mostly stable during this interval. At this MLT, the background counts of electrons at 1 keV are smoothly varying so that the inner edge and polar cap boundaries are not clear, which is consistent with *Elphic et al.* [1999].

4. Statistics

[16] Based on case studies such as discussed above, statistical analyses are presented in this section. Here we use data obtained between 12 March 2001 and 28 June 2002. As we have data for more than 1 year, the full range of MLT is covered. Measured electric fields are mapped to the magnetic equator using the magnetic field model of *Tsyganenko and Stern* [1996] for each 5 min interval, assuming equipotential magnetic field lines. The mapped locations when EDI data were available are shown in the top panel of Figure 3. As we are interested in the electric field in the inner magnetosphere, only periods with $L < 10$ are selected; Cluster perigee is $L \sim 4$. As seen from the figure, the spacecraft orbit covered all regions well and is sufficient for good statistics, although the coverage is somewhat less at ~3 MLT. The bottom panel shows MLAT for each L value at in situ locations of spacecraft. As L value becomes larger, the absolute values of MLAT increase.

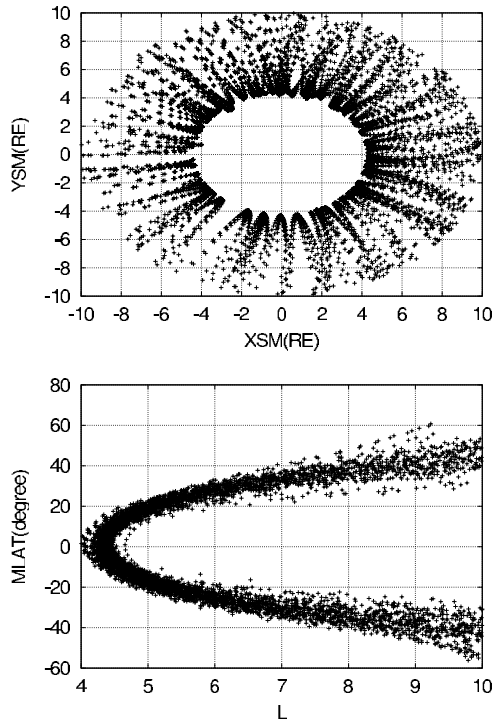

Figure 3. Cluster locations during which EDI data are available mapped to the equator by Tsyganenko model (top panel). The relation between L value and MLAT at the in situ spacecraft location (bottom panel).

[17] The 5 min averaged data sets are binned with a size of $\Delta L = 1$ for L value and 1 hour for MLT. The data are also sorted by the polarity of the 40 min averages of the IMF B_Z component, after propagation delay is taken into account. The time interval of 40 min is the same as that chosen by *Weimer* [2001]. (The calculated values are also available as supplemental material).[1] The average Kp index for IMF $B_Z > 0$ is 1.45, while that for IMF $B_Z < 0$ is 2.45. The latter indicates that our average southward IMF condition is quiet compared with stormtime conditions.

[18] Figures 4a and 4b show the number of 5 min averages in each bin, sorted by MLT on the horizontal axis, with L value shown by several line types. The figures are shown for each polarity of IMF B_Z. The number of data increases as L value decreases, indicating that the spacecraft stay a longer time at lower L shells. The larger number of samples between $MLT \sim 15$ and 24 is due to the fact that in the 15 month data set this MLT region is covered twice, in 2001 and 2002. Figures 4c and 4d show the average number of 2 s data used for the 5 min averages. In the absence of data gaps, the number of 2 s samples in 5 min would be 150. The average number decreases as L value increases, although the dependence is not as clear as in Figures 4a and 4b. When IMF $B_Z < 0$, the number of the nightside data is less than that of the dayside data at $L = 9.5$. One possible reason for such a difference is that fewer electron beams tend to return to the detector when the background magnetic field is smaller because the electron gyroperiod is longer and the beam dispersion is greater. Another reason is that the electric fields are more variable in the plasma sheet as shown in the case study in Figure 1 and reported by, e.g., *Quinn et al.* [2001]. In this case, tracking of the electron beams is harder than for more stable electric fields.

[19] Based on these data sets, two types of figures are shown for statistical averages: (1) the electric field magnitude and convection direction in the X-Y plane and (2) the dependence of the electric field on MLT at fixed L values. Figure 5 shows the electric field with the former style. Because of the large dynamic range of $\boldsymbol{E}$ and $\boldsymbol{V} = \boldsymbol{E} \times \boldsymbol{B}/B^2$, we show the vector data as a hybrid, $|E|\boldsymbol{V}/|V|$. In this figure the length of the vector corresponds to the magnitude of the electric field. An electric field of 0.2 mV/m corresponds to 1 R_E in the figure. The direction of the plotted vector is that of convection so that the direction of the electric field is obtained by rotating 90° in a counterclockwise direction. Figures 5a and 5b correspond to the cases with IMF $B_Z < 0$, while Figures 5c and 5d correspond to the cases with IMF $B_Z > 0$. The data are shown in both the corotating frame in Figures 5a and 5c and in the inertial frame in Figures 5b and 5d. For the case with IMF $B_Z < 0$, strong westward convection is observed in the duskside (Figure 5a). Such a region exists at $L = 4 \sim 10$ and at $14 \sim 20$ MLT. A dawn-dusk asymmetry of the electric field strength is clearly seen, which is consistent with previous work, e.g., by *Baumjohann and Haerendel* [1985]. In the inertial frame (Figure 5b), the corotating component is dominant at low L values. The polarity of the azimuthal convection is reversed at $L \sim 6$ in the evening MLT because the dawn-dusk and corotation electric fields have opposite signs. The stagnation point, at which the electric field is ~0, is located in this area. On the other hand, the dawn-dusk and corotation fields have the same sign on the dawnside so that eastward convection is observed at all L. On the dayside, sunward convection is observed. Magnetic flux is convecting toward the magnetopause, which might be related to the dayside reconnection. For IMF $B_Z > 0$ (Figure 5c), the convection in the corotating frame is much smaller than for IMF $B_Z < 0$ (Figure 5a). Westward convection in the duskside is smaller. Sunward convection on the dayside is also smaller in Figure 5d, presumably because less magnetic flux is transported to the tail from the magnetopause during reduced reconnection. The stagnation point is located at $L \sim 7.5$ with an accuracy of ± 1 R_E (our bin size) so that the size of the plasmasphere is expanded for northward IMF.

[20] Next we show statistical results more in detail at fixed L value (Figure 6). The electric field is shown in the corotating frame with a horizontal axis of MLT. Measurements from Cluster are shown as a solid line. The standard deviation is indicated as error bars. Results from previous observations are overlaid as noted in the legend: ground radar measurements by *Wand and Evans* [1981] (orange), *Volland* [1973] - *Stern* [1975] model (red), *Weimer* [2001] model derived from probe measurements on DE 2 (light blue), *McIlwain* [1986] E5D model from the particle measurements on ATS-5 (dark blue), and measurements by the Geos 2 electron beam instrument from *Baumjohann and Haerendel* [1985] (green). Radar data are mapped to the magnetic equator by assuming a dipole magnetic field at 56° MLAT (i.e., to $L \sim 3.2$). For the Volland-Stern model,

[1] Supporting data tables are available at ftp://agu.org/apend/ja/2003ja009913.

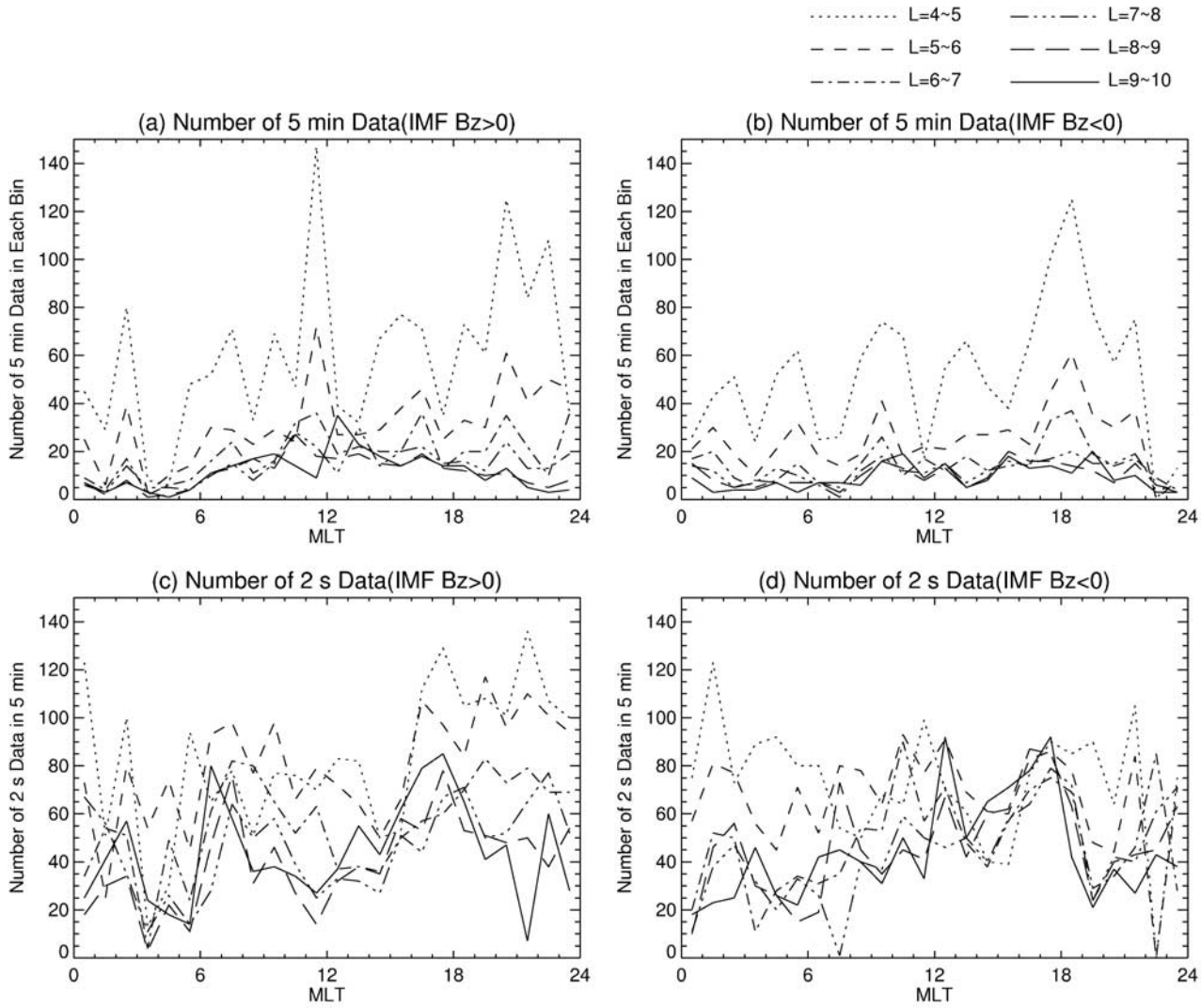

Figure 4. (a) and (b) Number of 5 min data in each bin, which has a size of $\Delta L = 1$ for L value and 1 hour for MLT. (c) and (d) Average number of 2 s data in order to obtain 5 min averages. If there is no data gap, the number of data in 5 min is about 150. Figures 4a and 4c are for IMF $B_Z > 0$. Figures 4b and 4d are for IMF $B_Z < 0$.

the electric potential in the corotating frame is given by the following equation,

$$\Phi = AL^{\gamma} \sin \phi, \tag{1}$$

where A is contribution from the dawn-dusk convection field, γ is the shielding parameter and ϕ is MLT. The relationship between the above parameter A and Kp index was determined by *Maynard and Chen* [1975] for a case with $\gamma = 2$. This relationship was inferred from the location of the plasmapause. In evaluating A, we use the average Kp index for both IMF B_Z polarities. The Weimer potential is mapped to the equator using the *Tsyganenko and Stern* [1996] model. Average solar wind conditions are introduced to the models.

[21] In Figure 6a the electric field is shown for $4 < L < 5$ and IMF $B_Z > 0$. The radial component is inward at approximately 0200 $\sim$ 1500 MLT. The azimuthal component is eastward at 0500 $\sim$ 1200 MLT, while it is westward at other MLT. This observation by Cluster is similar to the result from *Wand and Evans* [1981] for the winter season, at least at dayside MLT. We consider this point further in the discussion. The discrepancy is larger for the Volland-Stern, Weimer, and McIlwain models.

[22] Figure 6b shows electric fields at the same L range ($4 < L < 5$) but for southward IMF, in the same format as Figure 6a. A strong outward electric field of magnitude $\sim$0.8 mV/m is observed at 1900 $\sim$ 2200 MLT, although standard deviations are comparable to average values. This signature is not observed in the northward IMF case. The average value is about half of that in the case study, presumably because data from several orbits are averaged. The Kp index for the case study is $3^{+} \sim 4^{-}$, while for statistical study it is 2.45. It should be also noted that the electric field observed by Cluster is larger than that of the other models. The discrepancy from the Volland-Stern model is not surprising because it does not take into account the effect of the polarization field within the inner edge of the plasma sheet but only the effect of the dawn-dusk

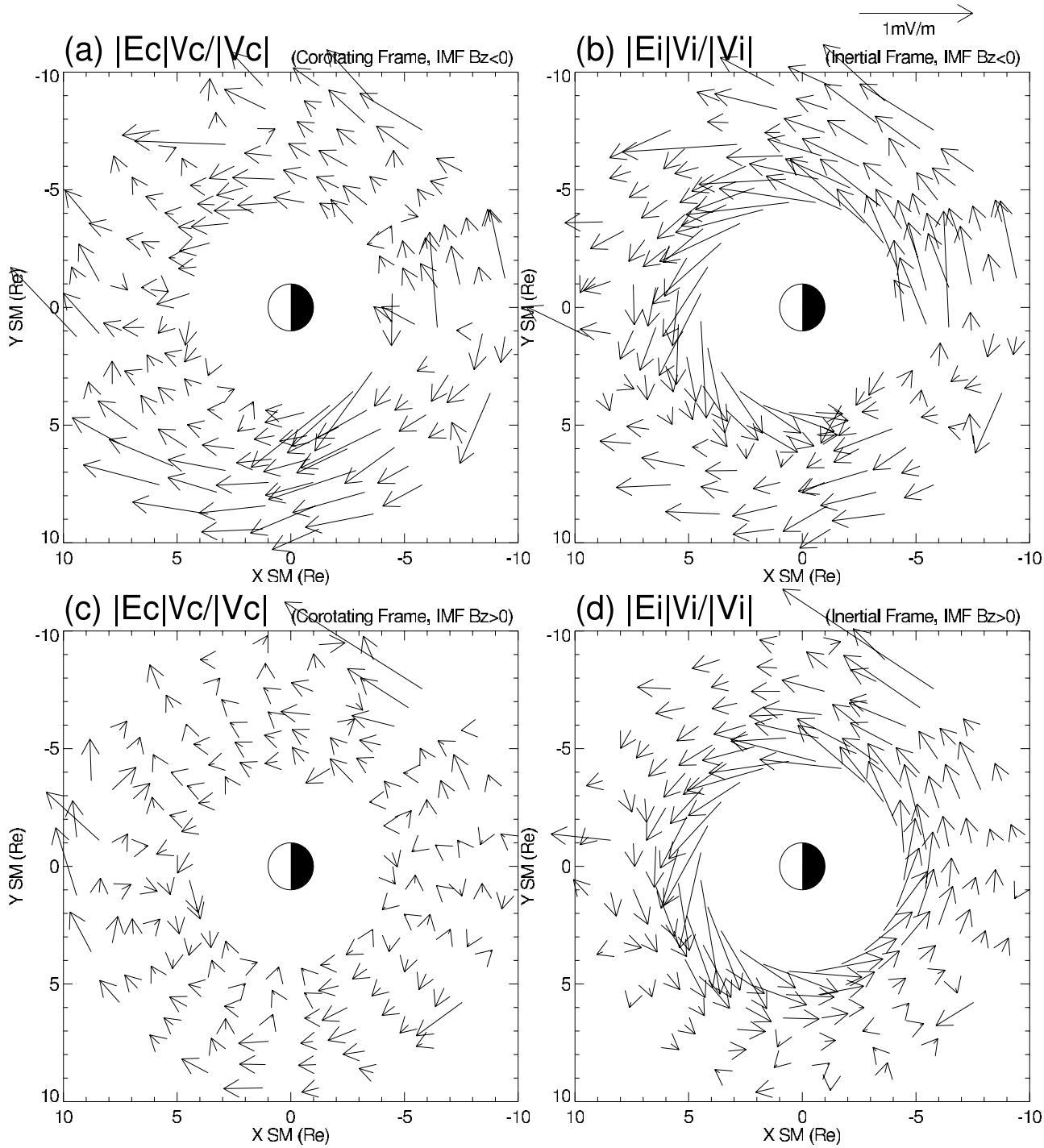

Figure 5. Electric field magnitude and convection direction in the X–Y plane. The length of the vector corresponds to the magnitude of the electric field. Electric field of 0.2 mV/m corresponds to 1 R_E in the figure. The direction of the plotted vector is that of convection, so that the direction of the electric field is obtained by rotating 90° in a counterclockwise direction. (a) and (b) Cases with IMF $B_Z < 0$. (c) and (d) Cases with IMF $B_Z > 0$. Figures 5a and 5c are shown in corotating frame, while Figures 5b and 5d are shown in inertial frame.

electric field. In the azimuthal component, the discrepancy between the Cluster observation and the other results is similar in size to that for the radial component.

[23] Figures 6c and 6d show electric fields for the southward IMF case but at $6 < L < 7$ and $9 < L < 10$, respectively. In Figure 6c a result from *Baumjohann and Haerendel* [1985] is overlaid. They obtained data from an electron beam instrument on Geos 2, somewhat similar to EDI. In this example, the electric fields from Cluster, Volland-Stern, Weimer, and *Baumjohann and Haerendel* [1985] are rather similar to each other, compared with the previous two examples. The electric field from the

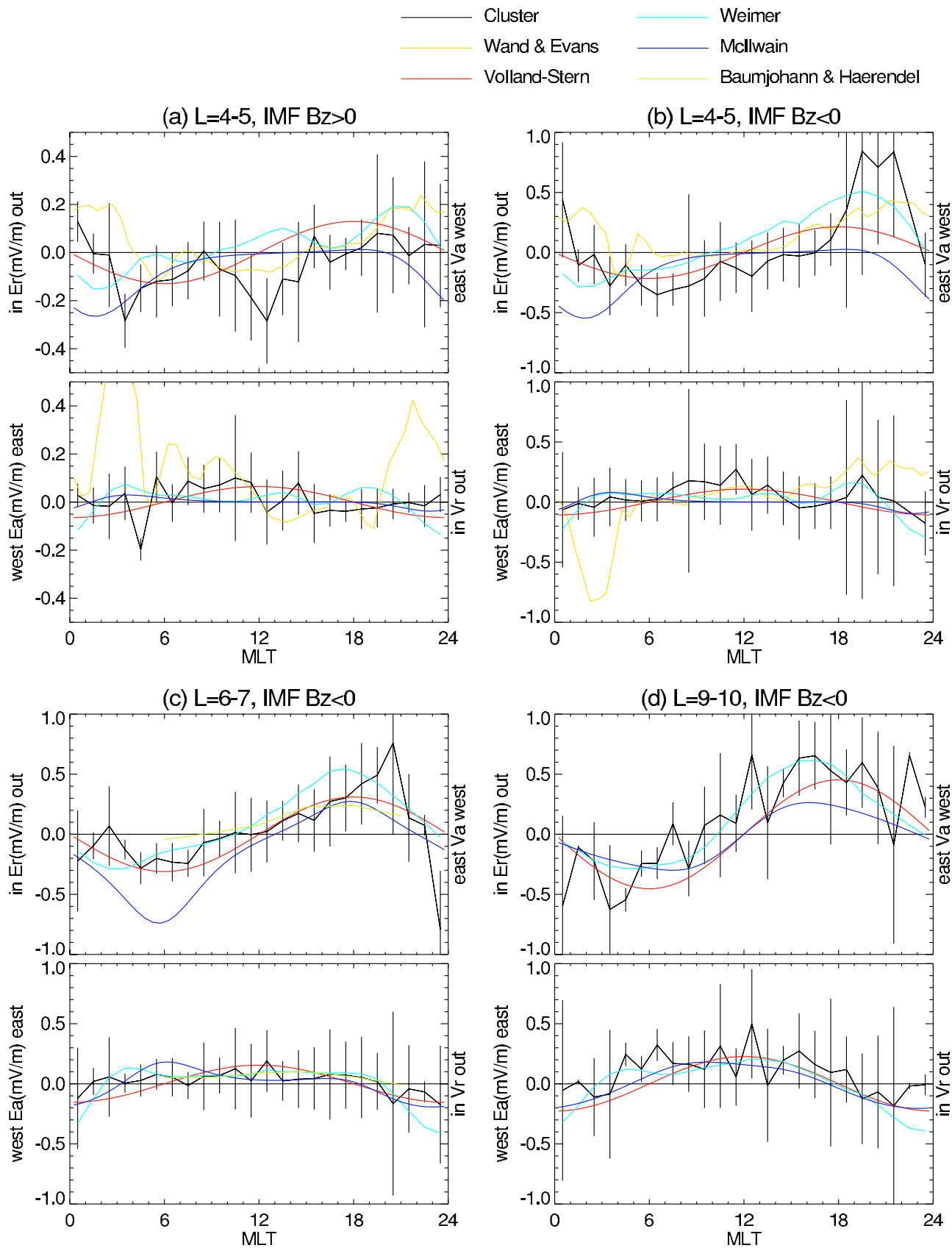
Cluster
Wand & Evans
Volland-Stern
Weimer
McIlwain
Baumjohann & Haerendel
(a) L=4-5, IMF Bz>0
(b) L=4-5, IMF Bz<0
(c) L=6-7, IMF Bz<0
(d) L=9-10, IMF Bz<0
in Er(mV/m) out
east Va west
west Ea(mV/m) east
in Vr out
MLT

McIlwain model has a larger negative value at predawn MLT than the other four. The largest outward electric field on Cluster is 0.7 mV/m at 20.5 MLT. A similar outward field appears in the Weimer model, although the peak local time is earlier at 17.5 MLT. The dawn-dusk asymmetry of the outward component is clear, which is also seen in Figure 5a. As for the azimuthal electric field, an eastward component is seen between 0100 and 2000 MLT, which agrees with the results from the Weimer and McIlwain models and *Baumjohann and Haerendel* [1985]. We note also that the radial component is generally larger than the azimuthal component. This might result from the shielding of the dawn-dusk electric field. When we consider the Volland-Stern model, the radial component E_R and azimuthal component E_A in the corotating frame are derived from equation (1) as follows:

$$(E_R, E_A) = \left(-\gamma A L^{\gamma-1} \sin\phi, -A L^{\gamma-1} \cos\phi\right) \quad (2)$$

If γ is above 1, then amplitude of radial component as a sinusoidal function of MLT is larger than that of azimuthal component, which is actually shown in Figure 6c.

[24] In Figure 6d, $9 < L < 10$ with southward IMF, the four electric fields are rather similar. However, the polarity of the EDI radial electric field changes at ~9 MLT, which is earlier than for the other three models and for lower L values. The latter point is similar to the theoretical calculation by *Vasyliunas* [1970], when the measured electric fields are mapped to the ionosphere. The direction of the electric field on the dayside is inward in the morning and early afternoon MLT at lower latitude where ionospheric conductivity is low, while it is outward in the late morning and afternoon MLT at higher latitude where ionospheric conductivity is high. Thus one possible explanation of the extension of the outward electric field toward the earlier MLT on Cluster is a gradient of ionospheric conductivity at $L = 4 \sim 10$. In this figure the radial component is again larger than the azimuthal component, indicating the shielding as in Figure 6c.

[25] Finally, we compare the average values and fluctuations. Here fluctuations are represented by standard deviations, which are the square root of the summation of the variances for two components in the X–Y plane. They are calculated from 5-min averages for each bin so that they do not include fluctuations with periods shorter than 10 min. Averages and standard deviations for $15 \sim 21$ MLT are shown in the inertial coordinate system (Figure 7). We chose this MLT range because it is where the stagnation point is expected to be located. At the stagnation point, the ratio of the AC electric field to the DC electric field is expected to be the largest. We have obtained one estimate of the statistical locations of the stagnation point from Figure 5. The locations are $L \sim 7.5$ for northward IMF and $L \sim 6$ for southward IMF. In Figure 7, standard deviations are often greater than the averages. This is true for $L > 7$ with northward IMF and for $L > 4$ with southward IMF. Locations of the stagnation point for both polarities of IMF B_Z are regions with larger standard deviations than the averages, therefore corotating plasma just inside the stagnation point might be easily relocated to the stream line connected to the magnetopause and vice versa. This indicates that the fluctuating component might result in the outflow of plasmaspheric material [e.g., *Matsui et al.*, 1999]. It should be also noted that the existence of the large fluctuating component is consistent with other previous reports [e.g., *Wygant et al.*, 1998; *Junginger et al.*, 1984; *Quinn et al.*, 1999].

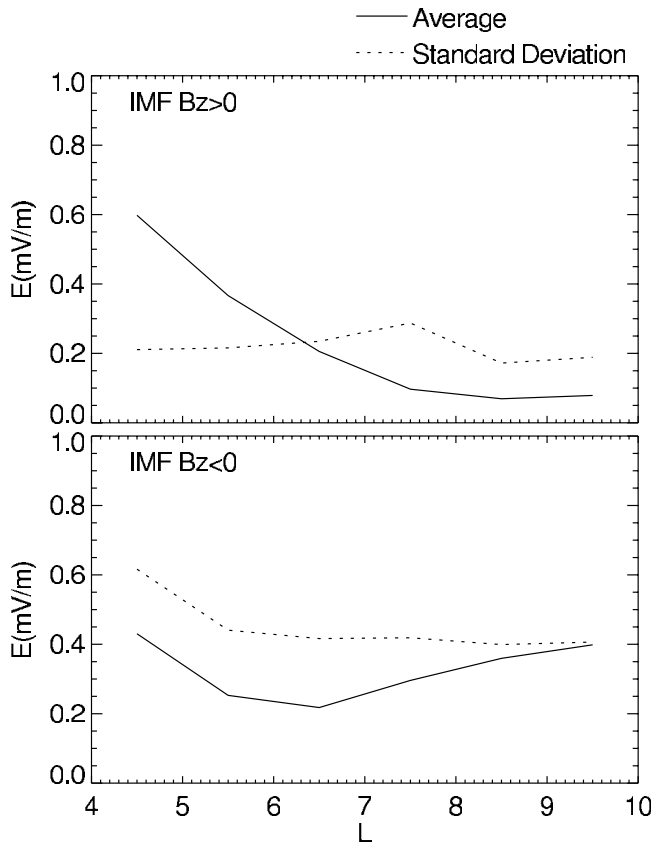

Figure 7. Averages and standard deviations of the electric field in the inertial frame for $15 \sim 21$ MLT. We chose this MLT range because the stagnation point is expected to be located.

5. Discussion

[26] In the above analysis, characteristics of the electric field measured by Cluster EDI are outlined. Here we discuss these results quantitatively and compare them with previous

Figure 6. (opposite) Dependence of the electric field in the corotating frame on MLT at fixed L values. Each panel shows the following cases: (a) $4 < L < 5$ and IMF $B_Z > 0$. (b) $4 < L < 5$ and IMF $B_Z < 0$. (c) $6 < L < 7$ and IMF $B_Z < 0$. (d) $9 < L < 10$ and IMF $B_Z < 0$. Data from Cluster are shown as a solid line. Standard deviation is indicated by error bars. Results from previous observations are overlaid as indicated in the legend: ground radar measurement by *Wand and Evans* [1981] (orange), *Volland* [1973] - *Stern* [1975] model (red), *Weimer* [2001] model derived from probe measurements on DE 2 (light blue), *McIlwain* [1986] E5D model from the particle measurements on ATS-5 (dark blue), and measurement by a beam instrument from *Baumjohann and Haerendel* [1985] (green).

models. The order of discussion starts from the region closer to the Earth. Thus our first concern is the contribution to the electric field by the ionospheric dynamo. Then, we estimate the component which results from the convection field.

[27] *Wand and Evans* [1981] assume the electric field at Millstone Hill is dominated by the effect of ionospheric dynamo during quiet activity. The similarity to the radar observation by *Wand and Evans* [1981] in the winter season suggests the possibility that the electric field measured by Cluster is strongly affected by the ionospheric dynamo at $L = 4.5$ with northward IMF. This idea is similar to what *Baumjohann et al.* [1985] suggested for the contribution of the ionospheric dynamo to the convection data from Geos 2 for quiet times. However, there are three more effects we should take into account: (1) The electric fields at nightside MLT do not agree with each other, which might result from larger error bars on the nightside as mentioned by *Wand and Evans* [1981]. (2) Discrepancy from the radar results at other seasons, such as summer and equinoxes, is larger. (See Figure 4 of *Wand and Evans* [1981].) (3) The latitude of the radar observation is lower by $\sim 6^\circ$ than the latitude of the footprint of Cluster at $L = 4.5$. In another work by *Heelis and Coley* [1992] they decomposed the radial electric field into Fourier components using data from DE 2. Diurnal components have different phase values depending on whether their origin is the magnetosphere or the ionosphere. A peak positive value for the magnetospheric component is at $\sim$19.5 MLT, while that for the ionospheric component is at $\sim$1100 MLT. Semidiurnal and terdiurnal components seem to result from the ionospheric dynamo. As for the phase of the diurnal component of Cluster data at $L = 4.5$, the peak positive value is $\sim$2100 MLT, which is similar to that attributed to a magnetospheric origin for DE 2. This suggests that the primary source of the diurnal components on Cluster is the magnetosphere. There is one additional reason regarding this point. As noted in the statistics, the boundary of the reversal of the sign of the radial components continuously moves toward later MLT with decreasing L values. Such electric field variation is similar to the simulation result by *Vasyliunas* [1970], which considered electric fields only with a magnetospheric origin. However, the radial electric field observed by Cluster is not sinusoidal because contributions from semidiurnal and terdiurnal components are not negligible. Here we should note that the amplitudes of the diurnal, semidiurnal, and terdiurnal components are obtained as 0.094, 0.044, and 0.072 mV/m, respectively, from the Fourier analysis. The origin of the latter two components might be the ionosphere as *Heelis and Coley* [1992] argued for the electric field at middle latitudes. Moreover, as noted in the statistics, Cluster observations are in better agreement with the radar observation than with the Volland-Stern and Weimer models, which supports the idea that the Cluster observations are affected by the ionospheric dynamo because these two models do not include its effect. From the amplitudes of the sinusoidal variations as shown, we can determine the percentage of the spectral power of the electric field of the magnetospheric origin and of the ionospheric origin to the spectral power of the total electric field. The magnetospheric percentage is at least $\sim$30% by assuming contribution from the diurnal component. The ionospheric percentage is at least $\sim$25% by assuming contribution from the semidiurnal and terdiurnal components. In summary, we infer that the electric field at $L = 4.5$, under northward IMF, is affected by both magnetospheric and ionospheric components. The former is observed as diurnal components of the radial electric field, while the latter is observed as semidiurnal and terdiurnal components.

Table 1. Averages and Standard Errors of γ Determined From Cluster Data

MLT range	γ for IMF $B_Z > 0$	γ for IMF $B_Z < 0$
Whole MLT	2.2 ± 0.5	1.6 ± 0.4
1500 $\sim$ 2100 MLT	2.5 ± 0.2	1.9 ± 0.3
0300 $\sim$ 0900 MLT	1.9 ± 0.7	1.3 ± 0.4

[28] Electric fields with a magnetospheric origin are shielded at lower L values as shown in the previous section. Here we try to determine the shielding parameter γ from the observation. A determination of γ was first given by *Volland* [1973]. He estimated γ as 2 because the shape of the plasmapause fits well with this value. *Baumjohann and Haerendel* [1985] estimated γ as 2 by using the ratio of radial to azimuthal components at geosynchronous orbit. On the other hand, *Kaye and Kivelson* [1981] determined γ by using dependence of the electric field on L value as follows. The parameter γ varies inversely with Kp for $Kp \lesssim 3$, and $\gamma \sim 1$ for $Kp \lesssim 3$. When geomagnetic activity is large, Kp 7, γ is inferred as negative, according to the radial dependence of electric field presented by *Rowland and Wygant* [1998]. This indicates that the shielding tends to disappear at high geomagnetic activity. We can estimate γ in a fashion similar to these works. From the data base we have shown, the dependence of the total electric field on L, averaged for all MLT ranges, is available. Here we average data over all MLT ranges, in order to discuss general characteristics first. Then the values for limited MLT ranges are discussed in the next paragraph. The parameter γ is estimated as 2.2 ± 0.5 for IMF $B_Z > 0$ and 1.6 ± 0.4 for IMF $B_Z < 0$, where we show averages and standard errors. The following equation is used to estimate γ:

$$\gamma = 1 + \sum_{L=4.5}^{9.5} \left(\frac{\log\left(\sqrt{\overline{|E_R|}^2 + \overline{|E_A|}^2}/C \right)}{\log L} \right) \Big/ 6, \qquad (3)$$

where $\overline{|E_R|}$ and $\overline{|E_A|}$ are the averages of the absolute values of the radial and azimuthal electric fields in mV/m in all MLT ranges, respectively. The offset C of the regression line is proportional to the cross-tail potential. The summation is between $L = 4.5$ and 9.5 with an interval of $\Delta L = 1$ so that it is divided into six L ranges. (We summarize estimated γ values in Table 1.) Although the standard error is large, the average value of γ is smaller with southward IMF. This is consistent with the result of *Kaye and Kivelson* [1981], indicating a tendency of weaker shielding as the activity increases. We note that activity is stronger with southward IMF. Moreover, the point that the average γ is close to 2 is consistent with *Volland* [1973] and *Baumjohann and Haerendel* [1985]. This value is not consistent with the value during the active period estimated from *Rowland and Wygant* [1998] because our average Kp index for both polarities of IMF B_Z is much smaller than that of stormtime periods. The above methods to estimate γ can also be applied

to the model by *Weimer* [2001]. In this case, γ is estimated as 2.33 ± 0.02 for IMF $B_Z > 0$ and 1.36 ± 0.04 for IMF $B_Z < 0$. Such values are close to those from Cluster observations shown above. Small values of the standard error result from the smoothed model with a limited order of spherical harmonic expansion. By using equation (3), it is possible to determine the cross-tail potential from Cluster data as well as γ. If we assume a magnetopause radius of 15 R_E at $x = -15$ R_E, the potential is estimated as 38 kV (108 kV) for IMF $B_Z > 0$ (IMF $B_Z < 0$). When we refer to, for example, *Weimer* [2001], such a value of the potential is typical.

[29] We now consider the dawn-dusk asymmetry of the electric field in the corotating frame. *Baumjohann and Haerendel* [1985] mentioned one reason for this as the different level of shielding of the dawn-dusk electric field at different MLT. Here we can estimate the γ dependence on MLT by using equation (3), although the MLT ranges to calculate averages must be modified. Choosing duskside MLT between 1500 and 2100 MLT, γ is estimated as 2.5 ± 0.2 (1.9 ± 0.3) for IMF $B_Z > 0$ (IMF $B_Z < 0$). For dawnside MLT between 0300 and 0900 MLT, γ is estimated as 1.9 ± 0.7 (1.3 ± 0.4) for IMF $B_Z > 0$ (IMF $B_Z < 0$). (These values are summarized in Table 1.) This indicates that larger shielding on the duskside is observed by Cluster. When shielding is effective, the field lines do not penetrate to the region close to the Earth. In the most simple case, the plasmasphere is completely shielded from the magnetospheric electric field, namely a perfect conductor. If the number of equipotential contours connecting from the magnetotail to the duskside magnetosphere is the same as that to the dawnside magnetosphere, the interval between the contours becomes narrower at the duskside because the distance between the magnetopause and the plasmapause is smaller at the duskside due to the plasmaspheric bulge. As a result, the electric field at the duskside is stronger. In this case a larger positive electric charge is accumulated at the duskside plasmapause, which is a similar situation within SAPS [e.g., *Anderson et al.*, 2001].

[30] Now we consider the dependence of the transport of magnetic flux toward the magnetopause on the polarity of IMF B_Z. A clear dependence of the outward transport of magnetic flux on this polarity is reported by *Baumjohann and Haerendel* [1985]. It is possible to calculate the average rate of sunward transport of magnetic flux in the dayside magnetosphere between 0600 and 1800 MLT at $9 < L < 10$. The values in the inertial frame are 0.11 mV/m and 0.32 mV/m for IMF $B_Z > 0$ and for IMF $B_Z < 0$, respectively. The value for southward IMF is about three times the value for northward IMF. We can compare this southward value with the tangential electric field at the magnetopause. *Lindqvist and Mozer* [1990] estimated this from 205 magnetopause crossings as $\sim$0.4 mV/m, which is close to the value from Cluster.

[31] In this study, we discuss results based on EDI measurements. However, there are limitations of the instrument. As stated previously, the return rate of beams is smaller at larger L value and nightside MLT, where larger fluctuating components occur. Large fluctuations may also occur during stormtime periods, such as investigated by *Wygant et al.* [1998], in which electric fields determined by a probe instrument were compared with the in situ magnetic fields as well as *Dst* index. Another work by *Burke et al.* [1998] examined a relation between electric field measurements and particle measurements during a stormtime period. The effects of strongly fluctuating electric fields on EDI beam returns will tend to bias the statistical results in highly active periods. Quantifying this through comparisons with other Cluster measurements is the subject of a future study.

6. Conclusions

[32] In this study we report electric fields obtained at $L = 4 \sim 10$ by EDI on Cluster. Results are obtained in all MLT ranges, using data from more than 1 year. The data are mapped to the magnetic equator and organized by IMF B_Z polarity. The average *Kp* index for southward IMF is 2.45 which is quiet compared to that of stormtime periods. The following six points are derived from the data.

[33] 1. In northward IMF the signatures of magnetospheric and ionospheric dynamo components seem to coexist at the lowest L values. The magnetospheric source contributes at least $\sim$30% to the electric field, while the ionospheric dynamo contributes at least $\sim$25%.

[34] 2. The shielding of the dawn-dusk electric field is seen in two ways: (1) the electric field is larger at higher L values in the corotating frame and (2) the amplitude of the radial electric field is larger than that of the azimuthal component.

[35] 3. The electric field at the duskside is larger than that at the dawnside in the corotating frame. One reason for this asymmetry is the different shielding level caused by the existence of the plasmaspheric bulge at the duskside.

[36] 4. In dayside MLT, the sunward convection in the inertial frame depends on the polarity of IMF B_Z being larger for IMF $B_Z < 0$, presumably because magnetic reconnection takes place preferentially with IMF $B_Z < 0$. For IMF $B_Z < 0$, the magnetic flux tubes are supplied to the dayside magnetopause with a rate of 0.32 mV/m.

[37] 5. The direction of the radial electric field in the dayside MLT is inward in the morning and early afternoon MLT at lower L value, while it is outward in the late morning and afternoon MLT at higher L value. The gradient of ionospheric conductivity might account for this observation.

[38] 6. The fluctuating electric field component is often larger than the average values. The fluctuating part might be important for transport of plasmaspheric material as well as radial diffusion of high-energy particles of the radiation belt. These effects will be investigated in future extensions of this work.

[39] **Acknowledgments.** We thank the many members of the EDI team for innumerable contributions to the design, development, and operation of EDI and to the ground processing of the data. HM thanks M. Chutter and B. Briggs for their continuous support on the software and data processing. R. Nakamura provided useful comments on the manuscript. We acknowledge D. R. Weimer for providing his model. Magnetic field and plasma data from ACE are provided through CDAWeb site by N. F. Ness and D. J. McComas, respectively. We are grateful to A. Balogh and the Cluster FGM team for providing the magnetic field data used by EDI onboard and in ground processing and to N. Cornilleau-Wehrlin and the STAFF team for providing the onboard STAFF data. This work was supported by NASA through grants NAG5-9960 and NAG5-13512.

[40] Arthur Richmond thanks Douglas E. Rowland and Daniel R. Weimer for their assistance in evaluating this paper.

References

Anderson, P. C., D. L. Carpenter, K. Tsuruda, T. Mukai, and F. J. Rich, Multisatellite observations of rapid subauroral ion drifts (SAID), *J. Geophys. Res.*, *106*, 29,585–29,599, 2001.

Axford, W. I., and C. O. Hines, A unifying theory of high-latitude geophysical phenomena and geomagnetic storms, *Can. J. Phys.*, *39*, 1433–1464, 1961.

Baumjohann, W., and G. Haerendel, Magnetospheric convection observed between 0600 and 2100 LT: Solar wind and IMF dependence, *J. Geophys. Res.*, *90*, 6370–6378, 1985.

Baumjohann, W., G. Haerendel, and F. Melzner, Magnetospheric convection observed between 0600 and 2100 LT: Variations with *Kp*, *J. Geophys. Res.*, *90*, 393–398, 1985.

Baumjohann, W., R. Nakamura, and G. Haerendel, Dayside equatorial-plane convection and IMF sector structure, *J. Geophys. Res.*, *91*, 4557–4560, 1986.

Blanc, M., and P. Amayenc, Seasonal variations of the ionospheric $E \times B$ drifts above Saint-Santin on quiet days, *J. Geophys. Res.*, *84*, 2691–2704, 1979.

Burke, W. J., N. C. Maynard, M. P. Hagan, R. A. Wolf, G. R. Wilson, L. C. Gentile, M. S. Gussenhoven, C. Y. Huang, T. W. Garner, and F. J. Rich, Electrodynamics of the inner magnetosphere observed in the dusk sector by CRRES and DMSP during the magnetic storm of June 4–6, 1991, *J. Geophys. Res.*, *103*, 29,399–29,418, 1998.

Carpenter, D. L., and N. T. Seely, Cross-*L* plasma drifts in the outer plasmasphere: Quiet time patterns and some substorm effects, *J. Geophys. Res.*, *81*, 2728–2736, 1976.

Carpenter, D. L., C. G. Parks, and T. R. Miller, A model of substorm electric fields in the plasmasphere based on whistler data, *J. Geophys. Res.*, *84*, 6559–6563, 1979.

Dungey, J. W., Interplanetary magnetic field and the auroral zones, *Phys. Rev. Lett.*, *6*, 47–48, 1961.

Elphic, R. C., M. F. Thomsen, J. E. Borovsky, and D. J. McComas, Inner edge of the electron plasma sheet: Empirical models of boundary location, *J. Geophys. Res.*, *104*, 22,679–22,693, 1999.

Foster, J. C., and W. J. Burke, SAPS: A new categorization for sub-auroral electric fields, *Eos Trans. AGU*, *83*(36), 393–394, 2002.

Galperin, Y. I., V. N. Ponomarev, and A. G. Zosimova, Plasma convection in polar ionosphere, *Ann. Geophys.*, *30*, 1–7, 1974.

Harvey, P., et al., The electric field instrument on the Polar satellite, *Space Sci. Rev.*, *71*, 583–596, 1995.

Heelis, R. A., and W. R. Coley, East-west ion drifts at mid-latitudes observed by Dynamics Explorer 2, *J. Geophys. Res.*, *97*, 19,461–19,469, 1992.

Heelis, R. A., W. B. Hanson, and J. L. Burch, Ion convection velocity reversals in the dayside cleft, *J. Geophys. Res.*, *81*, 3803–3809, 1976.

Heppner, J. P., Polar-cap electric field distributions related to the interplanetary magnetic field direction, *J. Geophys. Res.*, *77*, 4877–4887, 1972.

Heppner, J. P., and N. C. Maynard, Empirical high-latitude electric field models, *J. Geophys. Res.*, *92*, 4467–4489, 1987.

Jaggi, R. K., and R. A. Wolf, Self-consistent calculation of the motion of a sheet of ions in the magnetosphere, *J. Geophys. Res.*, *78*, 2852–2866, 1973.

Jordanova, V. K., C. J. Farrugia, L. Janoo, J. M. Quinn, R. B. Torbert, K. W. Ogilvie, R. P. Lepping, J. T. Steinberg, D. J. McComas, and R. D. Belian, October 1995 magnetic cloud and accompanying storm activity: Ring current evolution, *J. Geophys. Res.*, *103*, 79–92, 1998.

Jordanova, V. K., L. M. Kistler, C. J. Farrugia, and R. B. Torbert, Effects of inner magnetospheric convection on ring current dynamics: March 10–12, 1998, *J. Geophys. Res*, *106*, 29,705–29,720, 2001.

Junginger, H., G. Geiger, G. Haerendel, F. Melzner, E. Amata, and B. Higel, A statistical study of dayside magnetospheric electric field fluctuations with periods between 150 and 600 s, *J. Geophys. Res.*, *89*, 5495–5505, 1984.

Kaye, S. M., and M. G. Kivelson, The influence of geomagnetic activity on the radial variation of the magnetospheric electric field between $L = 4$ and 10, *J. Geophys. Res.*, *86*, 863–867, 1981.

Lindqvist, P.-A., and F. S. Mozer, The average tangential electric field at the noon magnetopause, *J. Geophys. Res.*, *95*, 17,137–17,144, 1990.

Matsui, H., T. Mukai, S. Ohtani, K. Hayashi, R. C. Elphic, M. F. Thomsen, and H. Matsumoto, Cold dense plasma in the outer magnetosphere, *J. Geophys. Res.*, *104*, 25,077–25,095, 1999.

Matsui, H., M. Nakamura, T. Mukai, K. Tsuruda, and H. Hayakawa, Observations of convection in the dayside magnetosphere by the beam instrument on Geotail, *Ann. Geophys.*, *19*, 303–310, 2001.

Maynard, N. C., and A. J. Chen, Isolated cold plasma regions: Observations and their relation to possible production mechanisms, *J. Geophys. Res.*, *80*, 1009–1013, 1975.

Maynard, N. C., T. L. Aggson, and J. P. Heppner, The plasmaspheric electric field as measured by ISEE 1, *J. Geophys. Res.*, *88*, 3991–4003, 1983.

McComas, D. J., S. J. Bame, P. Barker, W. C. Feldman, J. L. Phillips, P. Riley, and J. W. Griffee, Solar wind electron proton alpha monitor (SWEPAM) for the advanced composition explorer, *Space Sci. Rev.*, *86*, 563–612, 1998.

McIlwain, C. E., A K_p dependent equatorial electric field model, *Adv. Space Res.*, *6*(3), 187–197, 1986.

Melzner, F., G. Metzner, and D. Antrack, The Geos electron beam experiment S 329, *Space Sci. Instrum.*, *4*, 45–55, 1978.

Mozer, F. S., C. A. Cattell, M. Temerin, R. B. Torbert, S. Von Glinski, M. Woldorff, and J. Wygant, The dc and ac electric field, plasma density, plasma temperature, and field-aligned current experiments on the S3-3 satellite, *J. Geophys. Res.*, *84*, 5875–5884, 1979.

Nishida, A., Formation of plasmapause, or magnetospheric plasma knee, by the combined action of magnetospheric convection and plasma escape from the tail, *J. Geophys. Res.*, *71*, 5669–5679, 1966.

Noda, H., W. Baumjohann, R. Nakamura, K. Torkar, G. Paschmann, H. Vaith, P. Puhl-Quinn, M. Förster, R. Torbert, and J. M. Quinn, Tail lobe convection observed by CLUSTER/EDI, *J. Geophys. Res*, *108*(A7), 1288, doi:10.1029/2002JA009669, 2003.

Paschmann, G., et al., The electron drift instrument for Cluster, *Space Sci. Rev.*, *79*, 233–269, 1997.

Paschmann, G., et al., EDI electron time-of-flight measurements on Equator-S, *Ann. Geophys.*, *17*, 1513–1520, 1999.

Paschmann, G., et al., The electron drift instrument on Cluster: Overview of first results, *Ann. Geophys.*, *19*, 1273–1288, 2001.

Quinn, J. M., et al., EDI convection measurements at 5–6 R_E in the post-midnight region, *Ann. Geophys.*, *17*, 1503–1512, 1999.

Quinn, J. M., et al., Cluster EDI convection measurements across the high-latitude plasma sheet boundary at midnight, *Ann. Geophys.*, *19*, 1669–1681, 2001.

Rowland, D. E., and J. R. Wygant, Dependence of the large-scale, inner magnetospheric electric field on geomagnetic activity, *J. Geophys. Res.*, *103*, 14,959–14,964, 1998.

Smith, C. W., J. L'Heureux, N. F. Ness, M. H. Acuña, L. F. Burlaga, and J. Scheifele, The ACE magnetic fields experiment, *Space Sci. Rev.*, *86*, 613–632, 1998.

Stern, D. P., The motion of a proton in the equatorial magnetosphere, *J. Geophys. Res.*, *80*, 595–599, 1975.

Tsuruda, K., H. Hayakawa, M. Nakamura, T. Okada, A. Matsuoka, F. S. Mozer, and R. Schmidt, Electric field measurements on the Geotail satellite, *J. Geomagn. Geoelectr.*, *46*, 693–711, 1994.

Tsuruda, K., H. Hayakawa, and M. Nakamura, Electric field measurements in the magnetosphere by the electron boomerang technique, in *Measurement Techniques in Space Plasmas: Fields*, *Geophys. Monogr. Ser.*, vol. 103, edited by R. F. Pfaff, J. E. Borovsky, and D. T. Young, pp. 39–45, AGU, Washington, D. C., 1998.

Tsyganenko, N. A., and D. P. Stern, Modeling the global magnetic field of the large-scale Birkeland current systems, *J. Geophys. Res.*, *101*, 27,187–27,198, 1996.

Vasyliunas, V. M., Mathematical models of magnetospheric convection and its coupling to the ionosphere, in *Particles and Fields in the Magnetosphere*, edited by B. M. McCormac, pp. 60–71, D. Reidel, Norwell, Mass., 1970.

Vasyliunas, V. M., The interrelationship of magnetospheric processes, in *Earth's Magnetospheric Processes*, edited by B. M. McCormac, pp. 29–38, D. Reidel, Norwell, Mass., 1972.

Volland, H., A semiempirical model of large-scale magnetospheric electric fields, *J. Geophys. Res.*, *78*, 171–180, 1973.

Wand, R. H., and J. V. Evans, Seasonal and magnetic activity variations of ionospheric electric fields over Millstone Hill, *J. Geophys. Res.*, *86*, 103–118, 1981.

Weimer, D. R., Models of high-latitude electric potentials derived with a least error fit of spherical harmonic coefficients, *J. Geophys. Res.*, *100*, 19,595–19,607, 1995.

Weimer, D. R., An improved model of ionospheric electric potentials including substorm perturbations and application to the Geospace Environment Modeling November 24, 1996, event, *J. Geophys. Res.*, *106*, 407–416, 2001.

Wygant, J., D. Rowland, H. J. Singer, M. Temerin, F. Mozer, and M. K. Hudson, Experimental evidence on the role of the large spatial scale electric field in creating the ring current, *J. Geophys. Res.*, *103*, 29,527–29,544, 1998.

W. Baumjohann, Institut für Weltraumforschung der Österreichischen Akademie der Wissenschaften, Schmiedlstrasse 6, A-8042 Graz, Austria. (baumjohann@oeaw.ac.at)

V. K. Jordanova, H. Matsui, J. M. Quinn, and R. B. Torbert, Space Science Center, Morse Hall, University of New Hampshire, Durham, NH 03824, USA. (vania.jordanova@unh.edu; hiroshi.matsui@unh.edu; jack.quinn@unh.edu; roy.torbert@unh.edu)

G. Paschmann and P. A. Puhl-Quinn, Max-Planck-Institut für extraterrestrische Physik, P.O. Box 1603, D-85740 Garching, Germany. (gep@mpe.mpg.de; ppq@mpe.mpg.de)